CHEMISTRY

# Unprecedented stacking-dependent piezoluminescence enhancement in atomically precise superatomic gold nanoclusters

**Hua-Yang Ru[1]†, Ji-Kun Yang[1]†, Ya-Ni Yang[1], Qiu-Yang Wan[1], Meng-Jie Zhu[1], Jia-Hua Hu[1], Jing Li[2], Qi Li[3], Meng Zhou[4], Gang Li[1], Gaosong Chen[1]*, Yonggang Wang[5], Lei Jiang[6], Yuchen Wu[6], Shuang-Quan Zang[1]***



**Deciphering the structure-property relationship between cluster stacking and high-efficiency luminescence of metal nanoclusters is crucial for designing and synthesizing high-performance light-emitting materials and devices. Here, we successfully synthesized two polymorphic gold nanoclusters ($Au_8$-C and $Au_8$-P) and investigated their stacking-dependent piezoluminescence based on hydrostatic pressure. Under compression, $Au_8$-C exhibits notable piezoluminescence enhancement. However, $Au_8$-P presents monotonic piezoluminescence quenching. High-pressure structural characterizations confirm the existence of stacking-dependent anisotropic compression in $Au_8$-C and $Au_8$-P. Under high pressure, the columnar-stacked $Au_8$-C shrinks faster along the *a* axis, increasing the aspect ratio (AR) of the fusiform $Au_8$ core. However, the layered $Au_8$-P is compressed faster along the *c* axis, reducing the AR and leading to a flatter $Au_8$ core. High-pressure femtosecond transient absorption, time-resolved photoluminescence, and Raman spectra collaboratively confirm that differentiated anisotropic compression notably suppresses nonradiative loss caused by low-frequency vibrations of the $Au_8$ core, which is responsible for the piezoluminescence enhancement in $Au_8$-C.**

## INTRODUCTION

Superatomic Au nanoclusters (Au NCs) with closed-shell electronic structures typically exhibit excellent structural stability and have broad application prospects in sensing, catalysis, optical imaging, and biomarkers (*1*–*5*). However, because of the strong low-frequency vibrations and notable vibrational degrees of freedom of the metal core, superatomic Au NCs typically display low photoluminescence quantum yields (PLQYs) (*6*, *7*), which severely hinders their practical applications. To improve the PLQYs of superatomic Au NCs, strategies such as ligand engineering (*8*–*13*) and heterometallic doping (*14*–*19*) have been developed. By designing and assembling rigid staple motifs and large sterically hindered ligands onto the surface of Au NCs, the nonradiative relaxation caused by molecular vibrations can be effectively suppressed, considerably improving the PLQYs of Au NCs. Introducing heterometallic atoms into Au NCs to increase their energy gap is also a very effective approach for enhancing the PLQYs of Au NCs. These developed methods have primarily focused on studying the structure-optical property relationships of single-molecule Au NCs in solution and have neglected the study of PLQYs of crystalline superatomic Au NCs (table S1). Crystalline Au NCs with high PLQYs have broad application prospects in high-efficiency displays and solid-state lighting. However, the relationship between the stacking mode of NC molecules and their PLQYs in crystalline Au NCs remains unknown.

To elucidate the effect of the stacking mode of cluster molecules on their PLQYs, polymorphic metal NCs have been developed. The so-called polymorphic metal NCs are clusters with the same chemical composition but different single-crystal structures (*20*, *21*). Polymorphic metal NCs usually show distinct physicochemical properties and are considered ideal models for studying the structure-property relationship in NCs (*22*, *23*). The stacking-dependent luminescence behavior of organic solid materials has been systematically investigated by designing and preparing different types of polymorphic organic single crystals (*24*–*28*). Because of the complexity of cluster synthesis and the lack of characterization techniques, the structure-property relationship of polymorphic Au NCs remains unclear. Therefore, it is necessary to urgently develop convenient and efficient strategies to solve the above mentioned key scientific problems. Hydrostatic pressure can be used as a powerful tool to tune the crystal structure, electronic structure, and physicochemical properties of materials by decreasing interatomic distances and manipulating the electron orbital overlap (*29*–*40*). The hydrostatic pressure effect has provided valuable insights into the structural transformation and luminescence enhancement of solution-phase monomolecular Au NCs, 2-phenylethylthiol-protected $Au_{25}$ and cyclohexanethiolate-protected $Au_{21}$ (*41*, *42*). Therefore, introducing hydrostatic pressure effects into crystalline polymorphic Au NCs is expected to systematically reveal the relationship between the stacking mode of Au NCs and their PLQYs.

Here, a pair of polymorphic superatomic $[Au_8(dppp)_4(C{\equiv}CPh)_2](NO_3)_2$ [dppp = 1,3-bis(diphenylphosphino)propane, $PhC{\equiv}C^-$ = phenylacetylene substituent] NCs were successfully synthesized by modulating the crystalline solvent system, which crystallize in the *C*2/*c* ($Au_8$-C

[1]Henan Key Laboratory of Crystalline Molecular Functional Materials, and College of Chemistry, Zhengzhou University, Zhengzhou 450001, P. R. China. [2]School of Science, Xuchang University, Xuchang 461000, P. R. China. [3]Ministry of Education Key Laboratory of Macromolecular Synthesis and Functionalization, Department of Polymer Science and Engineering, Zhejiang University, Hangzhou 310027, P. R. China. [4]Department of Chemical Physics, Hefei National Research Center for Physical Sciences at the Microscale, University of Science and Technology of China, Hefei 230026, P. R. China. [5]School of Materials Science and Engineering, Peking University, Beijing 100871, P. R. China. [6]Key Laboratory of Bio-inspired Materials and Interfacial Science, Technical Institute of Physics and Chemistry, Chinese Academy of Sciences, Beijing 100190, P. R. China.
*Corresponding author. Email: chengaosong@zzu.edu.cn (G.C.); zangsqzg@zzu.edu.cn (S.-Q.Z.)
†These authors contributed equally to this work.

NC) and $P2_1/n$ ($Au_8$-P NC) space groups, respectively. Under ambient conditions, $Au_8$-C (16%) and $Au_8$-P (20%) display comparable PLQYs. Using a series of in situ high-pressure experiments, we systematically elucidated the structure-property relationship between the stacking modes and PLQYs of $Au_8$ NCs. Under compression, $Au_8$-C presents remarkable pressure-induced emission enhancement behavior. When the pressure increases to 1.7 GPa, the PLQY of $Au_8$-C increases to a maximum of 76%. However, in the same pressure range, $Au_8$-P only shows pressure-driven emission decay. Angle-dispersive x-ray diffraction (ADXRD) results show that $Au_8$-C and $Au_8$-P undergo differential anisotropic compressions under high pressure. During compression, $Au_8$-C and $Au_8$-P shrink faster along the *a* and *c* axes, respectively. Before 1.7 GPa, $Au_8$-C shrinks rapidly along the *a* axis, resulting in a continuous increase in the aspect ratio (AR) of the kernel in $Au_8$-C, making the Au—Au bonds shorter and uniform. In contrast, under high pressure, the AR of the kernel in $Au_8$-P continues to decrease, and distortion increases. Raman spectra demonstrate that pressure notably suppresses the low-frequency vibrations of the kernel in $Au_8$-C. Time-resolved photoluminescence (TRPL) and transient absorption (TA) spectra collaboratively confirm that the nonradiative loss in $Au_8$-C is considerably reduced under pressure, which is responsible for the emission enhancement of $Au_8$-C. This study not only provides valuable insights into the relationship between stacking modes and the luminescence properties of superatomic NCs under pressure but also demonstrates the practical applicability of high-pressure studies in nanochemistry.

## RESULTS

In our work, by adjusting the crystallization solvent system, two crystalline polymorphs Au NCs that crystallize in $C2/c$ ($Au_8$-C) and $P2_1/n$ ($Au_8$-P) space groups, respectively, were successfully obtained (Fig. 1). In detail, by diffusing ether in a solution of $CH_2Cl_2/CH_3OH$ (v/v = 1/1) containing $Au_8$ NCs, $Au_8$-C crystals were obtained (*43*). By contrast, $Au_8$-P crystals were obtained by diffusing ether in $CH_2Cl_2$ containing $Au_8$ NCs (tables S2 to S4). To the naked eye, $Au_8$-C (purple) and $Au_8$-P (red) crystals have notably different colors. The analysis of single crystal x-ray diffraction data reveals that $Au_8$-C and $Au_8$-P have similar [core + *exo*]-type $Au_8$ frameworks composed of a bitetrahedral $Au_6$ core and two Au atoms attached at *exo* positions, which are decorated by four dppp and two $PhC{\equiv}C^-$ (fig. S1). $CH_3OH$ molecules are included in the lattice unit of $Au_8$-C, notably altering the cluster stacking in the unit cell and resulting in a different space group for $Au_8$-C compared to $Au_8$-P. The stacking patterns of $Au_8$-C and $Au_8$-P are shown in Fig. 2 (A and C), respectively. $Au_8$-C exhibits a columnar configuration along the *c* axis (Fig. 2B), whereas $Au_8$-P displays a lamellar arrangement along the same direction (Fig. 2D) (*44*). Along the *a* axis, $CH_3OH$ molecules are intercalated into a void formed by $Au_8$-C, some $CH_3OH$ molecules are connected to $Au_8$-C via C—H···O hydrogen bonding interactions (2.602 to 2.677 Å; fig. S2). Noncovalent interaction analysis (*45*) further demonstrates the presence of C—H···O hydrogen bonding interactions in $Au_8$-C (fig. S3). Thus, the formation of polymorphic superatomic $Au_8$ NCs may be mainly dictated by the C—H···O hydrogen bonding. Different molecular stacking patterns result in distinct intermolecular interactions in $Au_8$ NCs (fig. S4). $Au_8$-C displays C—H···π (2.769 to 3.052 Å) and π···π (3.655 to 3.664 Å) interactions (fig. S5A), whereas $Au_8$-P exhibits only C—H···π (2.782 to 2.996 Å) interactions (fig. S5B). This variation in molecular stacking also leads to minor differences in $Au_8$ cores, with Au—Au bond lengths ranging from 2.618 to 3.168 Å in $Au_8$-C and from 2.622 to 3.110 Å in $Au_8$-P. The well overlapping powder x-ray diffraction (PXRD) patterns of the as-synthesized samples and simulated single-crystal data confirm the crystal phase purity of $Au_8$-C and $Au_8$-P (fig. S6).

To investigate the optical properties of $Au_8$-C and $Au_8$-P crystals under ambient conditions, the absorption, PL, and TRPL spectra were measured. Absorption spectra show that the absorption peaks of $Au_8$-C and $Au_8$-P crystals are different, located at 528 and 519 nm, respectively, and both present isolated absorption bands, corresponding to characteristic energy gaps of 2.18 and 2.25 eV, respectively (fig. S7). The photoluminescence (PL) spectra of $Au_8$-C and $Au_8$-P crystals reveal that they both exhibit red emission (fig. S8) with slightly different emission centers at 697 nm (PLQY: 16%) and 687 nm (PLQY: 20%), respectively (fig. S9A). The TRPL spectra show that $Au_8$-C (3.6 μs) and $Au_8$-P (5.4 μs) crystals have microsecond-order lifetimes under ambient conditions (fig. S9B), indicating that both crystals have phosphorescence-type emission properties. To investigate the effect of low temperature on the optical properties of gold NCs, the temperature-dependent PL and TRPL spectra of $Au_8$-C and $Au_8$-P were performed. As the temperature decreases from 300 to 80 K, the marked enhancement of the PL intensity and much longer lifetimes can be observed for $Au_8$-C and $Au_8$-P (fig. S10), indicating a notable suppression of nonradiative relaxation, which is attributed to the suppression of ligand

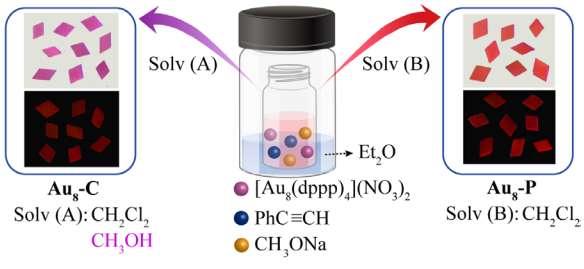


**Fig. 1. Synthetic route for $Au_8$-C and $Au_8$-P NCs.**

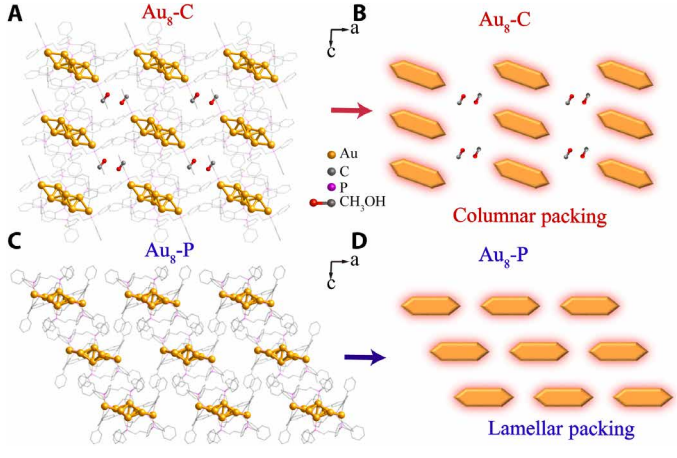


**Fig. 2. Single-crystal structures and simplified molecular stacking modes of $Au_8$-C and $Au_8$-P.** Single-crystal structures of (**A**) $Au_8$-C and (**C**) $Au_8$-P with hydrogen atoms omitted for clarity. The simplified molecular stacking modes of (**B**) $Au_8$-C and (**D**) $Au_8$-P are shown schematically.

vibrations at low temperatures. The consistent electrospray ionization mass spectrometry (fig. S11), absorption (fig. S12), emission spectra (fig. S13A), and decay lifetimes (6.35/6.40 ns; fig. S13B) of the solutions containing $Au_8$-C and $Au_8$-P indicate their consistency in the solution state. In addition, there were no obvious changes in absorption, emission, and Raman spectra within 25 days (fig. S14), indicating the well stability of the prepared crystals under ambient conditions.

To gain further insights into the intrinsic relation between the stacking mode of $Au_8$ NCs and their luminescent properties, in situ high-pressure PL, TRPL, and absorption spectra were performed. As shown in Fig. 3A, as the pressure increases, the PL spectra of $Au_8$-C display enhanced emission. When the pressure reaches 1.7 GPa, the PL intensity of $Au_8$-C is enhanced by more than six times compared with the initial intensity. Upon further compression, the PL signal of $Au_8$-C is gradually quenched (fig. S15). The PL photographs at different pressures demonstrate the change in emission brightness of $Au_8$-C and $Au_8$-P with pressure. By contrast, the emission intensity of $Au_8$-P continuously decreases with pressure (Fig. 3D). Meanwhile, the change in the emission of $Au_8$-C and $Au_8$-P was quantitatively evaluated in combination with their PLQYs under pressure (*46*). Figure 3C and fig. S16 show the variation trend of the PL intensity and PLQY of $Au_8$ NCs under pressure. At 1.7 GPa, $Au_8$-C exhibits the strongest PL intensity and its PLQY reaches a maximum of 76%. To elucidate the excited-state dynamics process of the PL evolution, the pressure-dependent TRPL spectra of $Au_8$-C and $Au_8$-P were collected. As shown in Fig. 3 (B and F), the average lifetime of $Au_8$-C increases from 3.6 to 6.6 μs when the pressure increases to 1.7 GPa. Thereafter, the PL lifetime of $Au_8$-C decreases (fig. S17), which is consistent with the trend of its PL signal under pressure. However, the average lifetime of $Au_8$-P only continuously decreases under pressure (Fig. 3E and fig. S18). The absorption spectra of $Au_8$-C and $Au_8$-P show that their absorption band edges are slightly red shifted with an increase in pressure and the energy gap value decreases (figs. S19 and S20), which is consistent with the change in the emission wavelengths of the corresponding PL spectra under pressure (fig. S21). Moreover, at different pressures, the absorption intensity of $Au_8$-C at an excitation wavelength of 450 nm does not show notable changes (fig. S22), indicating that the enhanced luminescence of $Au_8$-C is not contributed by changes in absorbance. After the pressure was completely released, the PL, absorption, and TRPL spectra of $Au_8$-C and $Au_8$-P are similar to those under ambient conditions, illustrating that compression and decompression processes are reversible (figs. S23 to S25). These results indicate that $Au_8$-C and $Au_8$-P exhibit stacking-dependent luminescence enhancement phenomena under pressure.

To reveal the correlation between stacking-dependent luminescence enhancement and structural evolution, in situ high-pressure ADXRD experiments were performed. As shown in Fig. 4 (A and D), with an increase in pressure, all diffraction peaks shift monotonically to higher diffraction angles, implying that pressure drives lattice contraction in $Au_8$-C and $Au_8$-P (tables S5 and S6). Meanwhile, no other notable peak or peak splitting was observed, indicating that no structural phase transition occurs in $Au_8$-C and $Au_8$-P under pressure. In addition, ADXRD can be reversibly returned to the initial test state, demonstrating that the structural changes of $Au_8$ NCs are reversible. The Rietveld refinement results for $Au_8$-C and $Au_8$-P at 1 atm and 1.7 GPa are shown based on ADXRD data. The

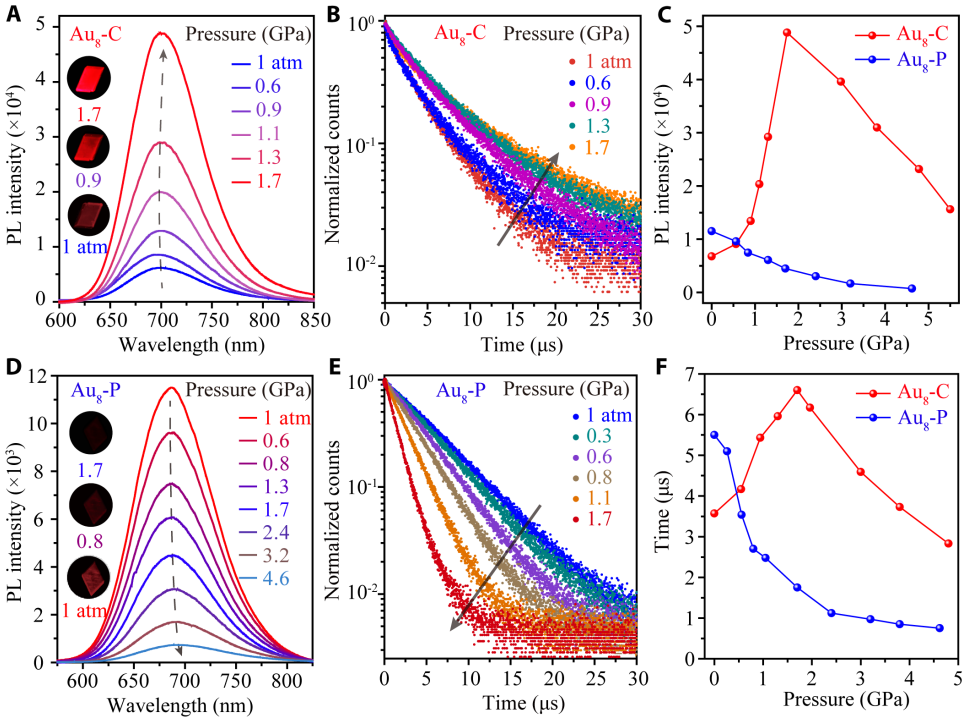


**Fig. 3. In situ high-pressure spectroscopic measurements of $Au_8$-C and $Au_8$-P.** In situ PL spectra of (**A**) $Au_8$-C and (**D**) $Au_8$-P crystals at different pressures. The illustrations show the optical micrographs of $Au_8$-C and $Au_8$-P at selected pressures. Pressure-dependent TRPL spectra of (**B**) $Au_8$-C and (**E**) Au8-P crystals. (**C**) PL intensity and (**F**) PL lifetime of $Au_8$-C and $Au_8$-P crystals as a function of pressure.

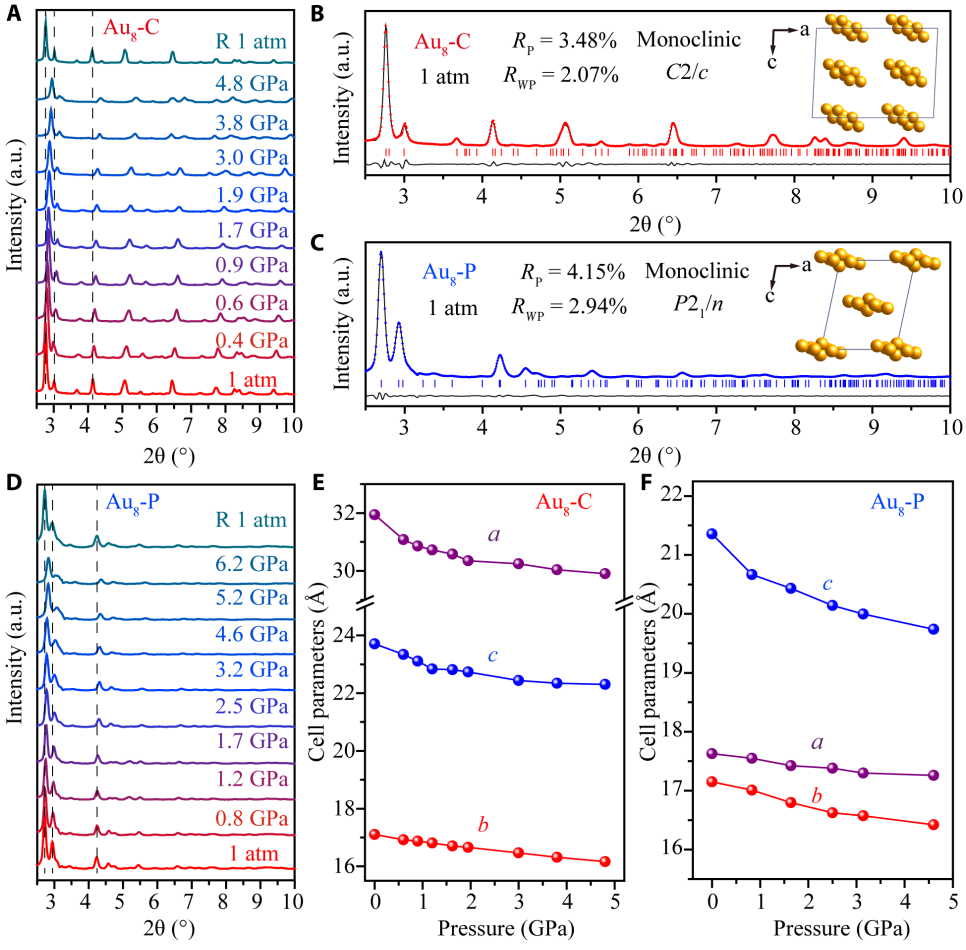


**Fig. 4. In situ structural characterization of $Au_8$-C and $Au_8$-P under high pressure.** In situ ADXRD patterns of (**A**) $Au_8$-C and (**D**) $Au_8$-P under pressure. Rietveld refinements of ADXRD patterns were collected at 1 atm of (**B**) $Au_8$-C and (**C**) $Au_8$-P. The insets show the corresponding molecular stacking modes in the monoclinic lattice. Pressure-dependence lattice parameters of (**E**) $Au_8$-C and (**F**) $Au_8$-P.

refinement results are in agreement with experimental data, confirming that $Au_8$-C and $Au_8$-P belong to the monoclinic crystal system at 1 atm and 1.7 GPa, corresponding to the *C*2/*c* and $P2_1/n$ space groups, respectively (Fig. 4, B and C, and fig. S26). The variations in the cell parameters of $Au_8$-C and $Au_8$-P upon compression are shown in Fig. 4 (E and F) and fig. S27. Under compression, $Au_8$-C and $Au_8$-P compress faster along the *a* and *c* axes, respectively. These considerably different anisotropic compressions may be closely related to their stacking modes. Figure S28 shows the variation in the cell volume of $Au_8$ NCs upon compression. Meanwhile, the relationship between the cell volume and pressure was fitted by the Birch-Murnaghan equation of state to obtain the bulk modulus ($B_0$) of $Au_8$-C (21.1 GPa) and $Au_8$-P (22.2 GPa) (fig. S29), indicating that the compressibilities of $Au_8$-C and $Au_8$-P are comparable (*47*, *48*).

To further reveal the intrinsic relationship between the stacking mode and optical properties of $Au_8$ NCs, the crystal structures of $Au_8$-C and $Au_8$-P at different pressures were optimized via density functional theory (DFT). For $Au_8$-C, as the pressure increases, the compression rate along the *a* axis is faster than that along the *b* and *c* axes (Fig. 5A). By analyzing the intercluster distances of $Au_8$-C along the *a*, *b*, and *c*axes (18.08, 14.53, and 19.40 Å), it was found that although the intercluster distance is largest along the *c* axis, the presence of stronger C—H···π and π···π intermolecular interactions result in larger steric hindrance, which is not favorable for compression (fig. S30). Because the intercluster distances along the *a* axis are relatively larger and there are no intermolecular interactions, contraction occurs more rapidly in $Au_8$-C. It is inferred that anisotropic compression correlates with the tightness of the cluster molecular stacking. Similarly, because the largest intercluster distance is along the *c* axis and intermolecular interactions are absent (fig. S31), $Au_8$-P exhibits an anisotropic compression tendency that makes it shrink faster along the *c* axis than *a* and *b* axes (Fig. 5B). Anisotropic compression strongly influences the distortion of the $Au_8$ core. As shown in Fig. 5C and fig. S32, under pressure, $Au_8$-C and $Au_8$-P tend to compress faster along the horizontal (*a* axis) and longitudinal (*c* axis) direction of the $Au_8$ core, respectively. To further quantify the structural deformation of $Au_8$ core under pressure, the distance between two $Au_{center}$ atoms in the longitudinal direction and two $Au_{exo}$ atoms in the horizontal direction were defined as $L_1$ and $L_2$, respectively (for illustrations see Fig. 5D). The change of $L_1/L_2$ (AR) (*49*) was used to represent the structural deformation of the $Au_8$ core (tables S7 and S8). Figure 5D shows that the AR of $Au_8$-C gradually increases during compression, reaching a maximum value of 0.275 at 1.7 GPa compared to 0.270 at 1 atm. Upon further compression,

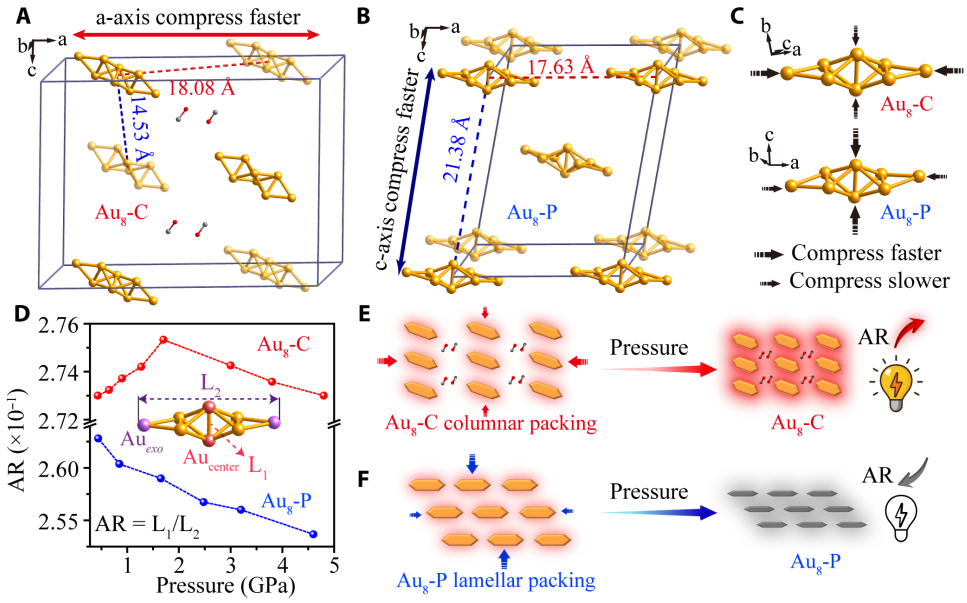


**Fig. 5. The evolution of anisotropic lattice compressibilities and core structure in $Au_8$-C and $Au_8$-P under pressure.** Anisotropic lattice compressibilities of (**A**) $Au_8$-C and (**B**) $Au_8$-P. (**C**) Anisotropic Au core compressibility of $Au_8$-C and $Au_8$-P. (**D**) Pressure-dependent the change in the AR of $Au_8$-C and $Au_8$-P. Schematic diagram of the stacking-dependent emission enhancement in (**E**) $Au_8$-C and (**F**) $Au_8$-P crystals under pressure.

the AR value of $Au_8$-C gradually decreases. By contrast, the AR of $Au_8$-P decreases monotonically under pressure. Therefore, the relationship between the structural evolution and optical properties of $Au_8$ NCs under pressure can be inferred as follows: When pressure is applied to $Au_8$ NCs, different stacking modes lead to distinct deformation trends of the $Au_8$ core. When the AR value increases, the $Au_8$ core becomes more compact and the bond length becomes more uniform, leading to an improvement in the PLQYs (Fig. 5E). Conversely, as the AR value decreases, the $Au_8$ core becomes more flattened and the length of metallic bonds varies more differently, resulting in the gradual quenching of the PLQYs (Fig. 5F).

To further investigate the effect of pressure on the kernel structure of $Au_8$-C and $Au_8$-P, in situ high-pressure Raman spectra were performed. With an increase in pressure, the vibration peaks of $Au_8$-C and $Au_8$-P gradually blue shift due to continuous lattice contraction (Fig. 6, A and C). In the Raman spectra of $Au_8$-C, the vibrational peaks in the low-frequency region (72.8 and 131.4 $cm^{-1}$) are attributed to the asymmetric stretching vibrations and breathing modes of the $Au_8$ kernel (*50*). These vibration peaks gradually broaden as the pressure increases and almost disappear when the pressure reaches 1.7 GPa (Fig. 6, A and B), indicating that the degrees of freedom and low-frequency vibrations of the $Au_8$ kernel are notably suppressed. This is associated with the pressure-induced enhancement of the PLQYs of $Au_8$-C. However, below 2.0 GPa, the vibrational peaks of $Au_8$-P do not show notable changes, indicating that the vibrations of its $Au_8$ core are not easily suppressed by pressure (Fig. 6, C and D). The effect of pressure on ligand vibrations is also unknown; therefore, pressure-dependent high-frequency Raman spectra of $Au_8$-C and $Au_8$-P were collected (fig. S33). Upon compression, the intensity of the main Raman signals gradually decreases, indicating that the vibrations of the ligand in $Au_8$-C and $Au_8$-P are suppressed. To study the evolution of noncovalent interactions in $Au_8$ NCs under high pressure, in situ high-pressure IR spectra of $Au_8$-C and $Au_8$-P were obtained (fig. S34). In $Au_8$-C, the O—H stretching vibration [$\nu$(O—H)] shows an obvious redshift, indicating that the C—H···O hydrogen bonds are strengthened. The strengthening of hydrogen bonds may limit the benzene ring vibration and reduce the nonradiative loss, which contributes to the enhancement of piezoluminescence of $Au_8$-C. However, no notable redshift of the vibration peak was observed in $Au_8$-P, indicating that there was no strengthening of hydrogen bonds in $Au_8$-P.

To gain further insights into the underlying photophysical mechanism of the enhancement of PLQYs in $Au_8$ NCs under pressure, femtosecond transient absorption (fs-TA) spectra were performed on $Au_8$-C crystals at 1 atm and 1.7 GPa, respectively. Upon excitation with a 530-nm laser pulse, $Au_8$-C displays notable excited-state absorption signals in the 587- to 735-nm range (Fig. 6E and fig. S35). The TA dynamics of $Au_8$-C crystals at 1 atm and 1.7 GPa can be decomposed into three components via global fitting (Fig. 6, F and G), and their corresponding kinetic traces at 700 nm are shown in fig. S36. The ultrafast component $\tau_1$ of the $Au_8$-C crystals at 1 atm (5.38 ps) and 1.7 GPa (5.82 ps) may be assigned to internal conversion from $S_n$ to $S_1$ states, and the second decay time $\tau_2$ at 1 atm (29.01 ps) and 1.7 GPa (72.36 ps) may be ascribed to the structural relaxation of the $Au_8$-C crystal (*51*). The third decay process of $Au_8$-C is long-lived and exceeds the detection limit of the fs-TA. Combining these results with the microsecond lifetimes obtained by TRPL, the long lifetimes $\tau_3$ of $Au_8$-C crystals are assigned to the relaxation from the $T_1$ state to the ground state to emit phosphorescence. Above all, the notably longer $\tau_2$ of $Au_8$-C at 1.7 GPa (compared to its value at 1 atm) implies that its nonradiative relaxation is reduced under pressure (*52*, *53*), which is consistent with the suppression of the low-frequency vibrations of its kernel. The radiative decay rate ($k_r$) and nonradiative decay rate ($k_{nr}$) of $Au_8$ NCs under pressure were further calculated. According to equations

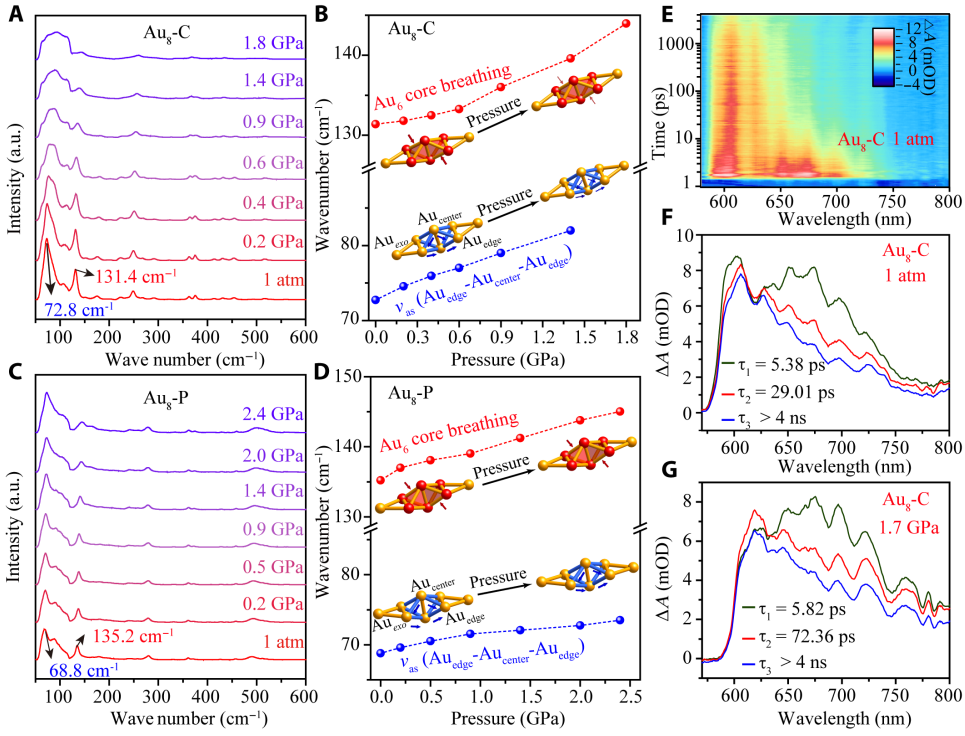


**Fig. 6. Raman spectra and excited-state dynamics of Au NCs under pressure.** Raman spectra of (**A**) $Au_8$-C and (**C**) $Au_8$-P at different pressures. Raman shift of (**B**) $Au_8$-C and (**D**) $Au_8$-P as a function of pressure. (**E**) Transient absorption data map of $Au_8$-C at 1 atm upon excitation at 530 nm. Evolution-associated spectra of $Au_8$-C at (**F**) 1 atm and (**G**) 1.7 GPa were obtained from global fitting on the TA data.

$$\mathrm{PLQY} = \frac{k_r}{(k_r + k_{nr})} \quad (1)$$

$$\tau = \frac{1}{k_r + k_{nr}} \quad (2)$$

Either increasing $k_r$ or reducing $k_{nr}$ will increase the PLQY. Based on the PLQY and lifetime data of $Au_8$ NCs, the $k_r$ and $k_{nr}$ rates at each pressure point were obtained. At 1.7 GPa, the $k_r$ rate of $Au_8$-C exhibits threefold, and the $k_{nr}$ rate declined sevenfold (table S9). However, $Au_8$-P only shows a decrease in $k_r$ and a rapid increase in $k_{nr}$ under pressure (table S10).

To further investigate the relationship between the electronic structure and optical properties of $Au_8$-C and $Au_8$-P, time-dependent DFT (TDDFT) calculations were performed. The simulated absorption spectra of $Au_8$-C (Fig. 7, A and D) and $Au_8$-P (fig. S37A) correlate well with experimental spectra, indicating the accuracy of computational results. The molecular orbitals [highest occupied molecular orbital (HOMO) and lowest unoccupied molecular orbital (LUMO)] of $Au_8$-C and $Au_8$-P present the typical superatomic configuration (fig. S38). To analyze the molecular orbital composition of $Au_8$-C and $Au_8$-P, the transitions of their molecular orbitals are presented in figs. S39 and S40. The isolated absorption peaks of $Au_8$-C (a) and $Au_8$-P (α) correspond to the transitions from the highest occupied molecular orbital to the lowest unoccupied molecular orbital (HOMO → LUMO). Notably, in $Au_8$-C, the LUMO distribution is more delocalized under high pressure than the initial orbital distribution (Fig. 7, C and F), which is correlated with enhanced luminescence (*54*). The Kohn-Sham molecular orbitals of $Au_8$-C (Fig. 7, B and E) and $Au_8$-P (fig. S37B) show that their HOMO and LUMO are predominantly constituted by Au (6sp) atomic orbitals. Therefore, the red luminescence of $Au_8$-C and $Au_8$-P originates from the metal-centered state. In addition, the hole-electron pairs of the $T_1$ state are mainly distributed on the kernels of $Au_8$-C and $Au_8$-P (figs. S41 to S44), further confirming metal-centered state luminescence. Meanwhile, the spin-orbit coupling constant (SOC) of $Au_8$-C is higher at high pressure than at 1 atm (Fig. 7H), which will contribute to the promotion of the intersystem crossing rate. However, the SOC of $Au_8$-P does not exhibit noticeable changes under pressure (fig. S46).

In summary, under high pressure, the different molecular stacking arrangements of $Au_8$-C and $Au_8$-P NCs lead to distinct anisotropic compression behaviors. The rapid shrinkage of the lattice *a* axis in $Au_8$-C leads to a more uniform Au—Au bond length in the $Au_8$ kernel, notably suppressing low-frequency vibrations and thus decreasing nonradiative loss. This is the source of the pressure-induced PL enhancement in $Au_8$-C (Fig. 7, G and H). However, the kernel of $Au_8$-P becomes more flattened under compression and its low-frequency vibrations are not considerably suppressed, resulting in pressure-induced PL quenching (figs. S45 and S46). To validate the correctness of the discovered stacking-dependent efficient luminescence mechanism, we designed and synthesized an eight-core Au NC, protected by the 4-ethynylbenzaldehyde ligand ($Au_8$-CHO), which displayed pressure-induced luminescence enhancement. The crystal structure of $Au_8$-CHO (fig. S47, tables S11 to S13) and its cluster molecular stacking pattern (fig. S48) are almost identical to those of $Au_8$-C. The pressure-dependent microscopic optical photos,

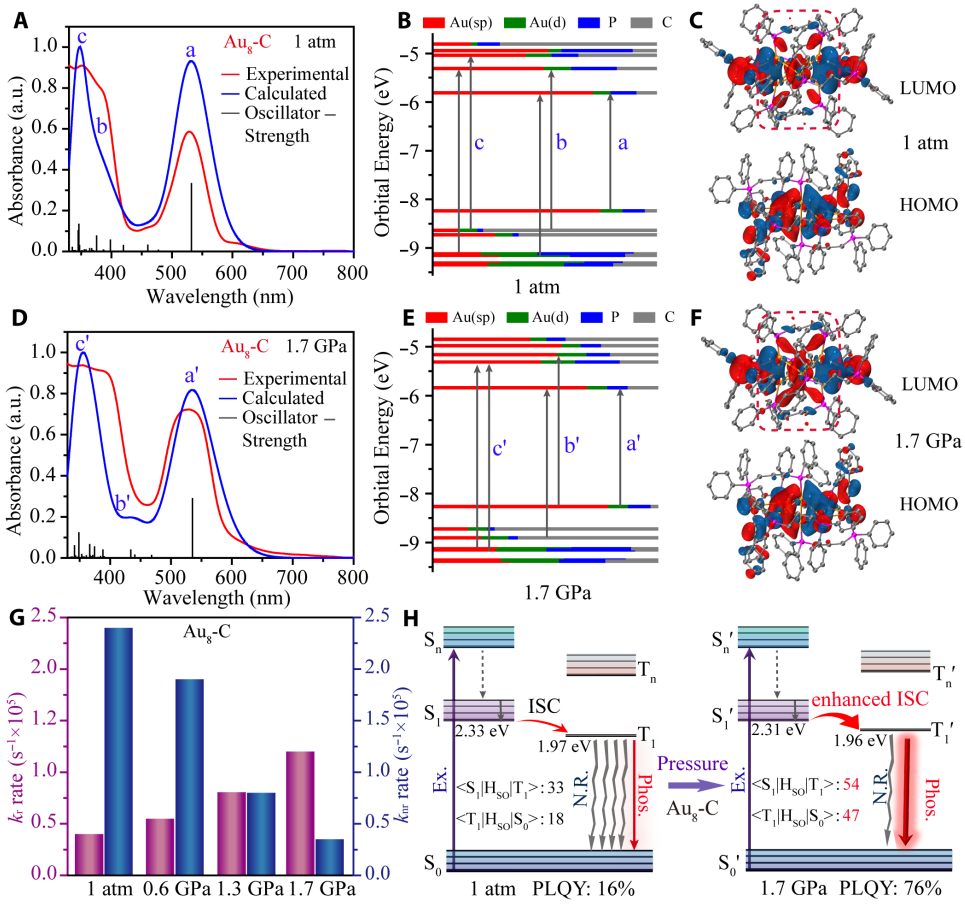


**Fig. 7. Pressure-induced PL enhancement mechanism of $Au_8$-C.** Experimental and calculated absorption spectra of $Au_8$-C at (**A**) 1 atm and (**D**) 1.7 GPa. The Kohn-Sham molecular orbital energy level diagram and associated populations of atomic orbitals in each molecular orbital for $Au_8$-C at (**B**) 1 atm and (**E**) 1.7 GPa. Frontier orbitals including the HOMO and LUMO of $Au_8$-C at (**C**) 1 atm and (**F**) 1.7 GPa. (**G**) Radiative and nonradiative recombination rates of $Au_8$-C at different pressures. (**H**) Schematic diagram of the PL mechanism of $Au_8$-C at 1 atm and 1.7 GPa. Ex., excitation; N.R., nonradiative; Phos., phosphorescence; a.u., arbitrary unit.

luminescence phenomenon, and Raman spectra of $Au_8$-CHO are similar to the evolution in the optical behavior of $Au_8$-C under high pressure (figs. S49 and S50). In addition, the $Au_8$-TPE (*55*) and $Au_8$-CzPA (*56*) were also synthesized to further confirm the piezoluminescence enhancement stemmed from NCs stacking in the unit cell. Upon compression, the packing arrangement of $Au_8$-TPE and $Au_8$-CzPA leads the lattice units to shrink faster along the *c* and *a* axes, respectively. Thus, the AR of $Au_8$-TPE and $Au_8$-CzPA show opposite changing trends under pressure (figs. S51 and S52). Ultimately, the $Au_8$-TPE exhibits the piezoluminescence enhancement, whereas $Au_8$-CzPA shows only pressure-induced luminescence quenching. The absove results further prove the correctness of our discovered structure-property relationship between the stacking mode and PLQYs.

## DISCUSSION

In conclusion, we designed and synthesized a pair of polymorphic superatomic Au NCs ($Au_8$-C and $Au_8$-P) and systematically elucidated the stacking-dependent efficient luminescence mechanism of metal NCs via the hydrostatic pressure effect and a series of in situ characterization methods. Under compression, columnar-stacked $Au_8$-C exhibits notable luminescence enhancement, with its PLQY reaching a maximum of 76% at 1.7 GPa, whereas lamellar-stacked $Au_8$-P only displays luminescence quenching. Pressure-dependent ADXRD results reveal that $Au_8$-C and $Au_8$-P show anisotropic trends with faster compression along the lattice *a* axis and *c* axis, respectively. The faster shortening of the *a* axis leads to a more compact core in $Au_8$-C, whereas the faster compression along the *c* axis results in a more flattened core in $Au_8$-P. TRPL, TA, and Raman spectra collaboratively demonstrated that pressure effectively suppresses the low-frequency vibrations of the kernel in $Au_8$-C, leading to a decrease in nonradiative loss. This suppression is responsible for the pressure-induced emission enhancement in $Au_8$-C. This study provides a deeper understanding of the relationship between cluster stacking and luminescence properties, providing valuable insights for designing highly efficient luminescent superatomic NCs in the future.

## MATERIALS AND METHODS

### Materials and reagents

All chemicals and reagents for synthesis were obtained from commercial sources and used without any further purification. $HAuCl_4{\cdot}4H_2O$ were purchased from Civic Chemical. The dppp (97%)

and sodium borohydride (99%) were purchased from Sigma-Aldrich. 4-ethynylbenzaldehyde (98%), 9-(4-ethynylphenyl)carbazole (98%), (2-(4-ethynylphenyl)ethene-1,1,2-triyl)tribenzene (96%), and phenylacetylene (98%) were purchased from Macklin. Methanol (99.5%), dichloromethane (99%), and ether (99%) were purchased from Macklin.

### Synthesis of $Au_8$-C and $Au_8$-P crystals

The $[Au_8(dppp)_4(C{\equiv}CPh)_2](NO_3)_2$ clusters were synthesized using $[Au_8(dppp)_4](NO_3)_2$ (*57*) as precursor. A methanolic solution (50 ml) of $[Au_8(dppp)_4](NO_3)_2$ (30.0 mg, 9 μmol) was added to phenylacetylene (2.0 μl, 18 μmol) and sodium methoxide (145 mg, 2.7 mmol), and the mixture was stirred at room temperature for 10 hours. The obtained mixture was treated with water and then extracted with dichloromethane (20 ml × 3). The organic phase was dried by anhydrous $Na_2SO_4$, filtered, and evaporated to dryness to give a pinkish solid; purified by recrystallization by vapor diffusion of ether into a dichloromethane/methanol (~50/50 v/v) solution to give $Au_8$-C as purple crystals; and purified by recrystallization by vapor diffusion of ether into a dichloromethane solution to give $Au_8$-P as red crystals. The synthesis yields of $Au_8$-C and $Au_8$-P are 46 and 48%, respectively. $Au_8$-CHO was prepared using the same synthetic route as described above, with the synthesis yield of 52%.

### Crystallographic data collection and structural refinement

Single-Crystal x-ray Diffraction (SCXRD) measurements of $Au_8$-P clusters were performed at 200 K on a Rigaku XtaLAB Pro diffractometer with Cu-Kα radiation (λ = 1.54184 Å). Data collection and reduction were performed using the program *CrysAlis$^{Pro}$* (*58*). The structure of $Au_8$-P was solved with direct methods (*SHELXS*) (*59*) and refined by full-matrix least squares on $F^2$ using *OLEX2* (*60*), which uses the *SHELXL-2015* module (*61*, *62*). All atoms were refined anisotropically, and hydrogen atoms were placed in their calculated positions with idealized geometries and assigned fixed isotropic displacement parameters. The detailed information of the crystal data and refinement results are summarized in table S2.

### Instrumentation

PXRD patterns of the samples were collected at room temperature in the air using a Rigaku MiniFlex diffractometer (Cu-Kα, λ = 1.54178 Å; 2θ range of 3° to 50°). Simulated powder patterns were obtained with Mercury software and a crystallographic information file from a single-crystal x-ray experiment. Mass spectra (MS) were recorded on an X500R QTOF spectrometer.

### Photophysical measurements

Absorption spectra were recorded using a Hitachi UH4150 ultraviolet-visible spectrophotometer in the range of 200 to 800 nm. PL spectra were recorded with a HORIBA FluoroLog-3 fluorescence spectrometer. TRPL decay spectra were measured on a HORIBA FluoroLog-3 fluorescence spectrometer equipped with a 370-nm laser operating in time-correlated single-photon counting mode. The PLQYs in the solid state were operated using an integrating sphere on the HORIBA FluoroLog-3 fluorescence spectrometer.

### High-pressure generation

High pressure was generated by a symmetric diamond anvil cell (DAC) through a pair of diamonds with 500-μm culet size. The $Au_8$-C, $Au_8$-P crystals, and a small ruby ball were loaded into the 180-μm-diameter hole of a DAC, which was made of a T301 steel gasket pre-indented to a thickness of 45 μm. All the high-pressure experiments used the silicon oil as a pressure transmitting medium (PTM). The PTM remains quasi-hydrostatic up to 4 GPa but can be safely used in the pressure range covered by this study (*63*) and did not have any detectable effect on the behavior of $Au_8$-C/$Au_8$-P crystals under pressure. All the experiments were conducted at room temperature.

### In situ high-pressure optical experiments

The in situ high-pressure PL spectra were measured using a 450-nm laser excitation. The PL micrographs were captured using an Olympus DP74 camera equipped on the microscope (Olympus BX53) with the same exposure time. High-pressure absorption experiments were carried out using the deuterium-halogen light source (Ocean Insight DH-2000-BAL) and a fiber spectrometer of Ocean Insight QEP03490. The TRPL spectra were measured in a PMA Hybrid spectrometer using a 450-nm picosecond laser with a resolution time of 512 ps. The Raman spectra were collected in a spectrometer (Princeton Instruments, HRS-500) with a cryogenic detector (Andor, iVac 316). The excitation source is a laser with a wavelength of 785 nm, and the grating used is 2400 lines/mm Bragg grating. In situ high-pressure ADXRD experiments were carried out at beamline 15 U1, Shanghai Synchrotron Radiation Facility (SSRF) >and 4 W2 HP-Station in the Beijing Synchrotron Radiation Facility (BSRF). Before high-pressure ADXRD measurements, $CeO_2$ was applied for calibration. The wavelength of the incident x-ray beam was adjusted to be 0.6199 Å. The one dimensional ADXRD spectra were obtained using the Dioptas software. All high-pressure experiments were conducted at room temperature.

The fs-TA measurements were carried out on a homebuilt pump-probe system used with a regeneratively amplified Ti:sapphire laser system (Coherent Legend Elite HE+USP-1 K-III, 35 fs, 1 kHz). The central wavelength of the output pulse is 800 nm, and the output pulse is split into two beams. The first beam passes through the optical parametric amplifier (Light Conversion, TOPAS Prime) to generate 530 nm. The second beam is focused on sapphire to produce continuous white light (from 450 to 1000 nm) for visible near-infrared detection. The time delay between the pump and probe pulse is controlled by the motorized delay stage. The transmission changes of the probe light were collected by a fiber spectrometer (AvaSpec-ULS2048CL-EVO, Avantes).

### Computational details

#### *DFT calculations*

All-electron DFT calculations have been carried out by the latest version of ORCA quantum chemistry software (*64*) (version 5.0.4). The calculated structures were built from their single-crystal structures. The position of the H atoms was optimized, and the other atoms kept their positions unchanged. The Perdew-Burke-Ernzerhof (PBE) functional (*65*) and the def2-SVP basis set (*66*) were adopted for geometry optimization calculation. The DFT-D3 dispersion correction with BJ damping (*67*, *68*) was applied to correct the weak interaction to improve the calculation accuracy. The excited states calculation and spin-orbit coupling (SOC) calculation were performed with TPSSH functional (*69*) and mixed basis set (SARC-DKH-TZVP basis set for Au atoms and DKH-def2-SVP basis set for other atoms). SOC calculation was performed by the spin-orbit mean-field method (*70*).

### *Theoretical calculation of weak interaction calculations*

The calculation was carried out using Gaussian 09 software package. First, the PBE/def2tzvp functional basis set was used to optimize the structure of $Au_8$-C cluster under normal pressure using DFT optimization only for hydrogen atoms. Then, based on the minimum structure of ground state, TPSSH/def2-SVP level TDDFT calculations were performed; Multiwfn software was used combined with VMD program to perform IGMH analysis, and the desired hydrogen bonds were drawn (*71*).

### *Refinements methods and procedures*

Pawley and Rietveld refinements of XRD patterns were accomplished using the Reflex module combined with the Materials Studio program. All Pawley and Rietveld refinements were performed using four refinement cycles and fine convergence criteria. First, the pattern was indexed by means of the peak picking option of the software package. Potential solutions for cell parameters were found using the X-cell methods. Then, a Pawley profile-fitting procedure was applied to refine cell parameters and search space groups. The final Rietveld refinement (including Pawley refined parameters, atomic positions, preferred orientations, and overall isotropic factor) was performed to obtain the crystal structural parameters. The quality of the fitting between the experimental and calculated profile is assessed by the various $R$ parameters like $R_p$ (profile factor) and $R_{wp}$ (weighted profile factor)

$$R_p = \left\{ \frac{\sum_i |I_i^{obs} - I_i^{cal}|}{\sum_i I_i^{obs}} \right\} \quad (3)$$

$$R_{wp} = \left\{ \frac{\sum_i w_i \left(I_i^{obs} - I_i^{cal}\right)^2}{\sum_i w_i \left(I_i^{obs}\right)^2} \right\}^{\frac{1}{2}} \quad (4)$$

where $I_i^{obs}$, $I_i^{cal}$, and "$i$" indicates the experimental, calculated, and total number of points, respectively, and the "$w_i$" is the reciprocal of the variance of observation $I_i^{cal}$.

### *Bulk modulus determination using the Birch-Murnaghan equation of state*

The pressure-volume ($P$-$V$) data were fitted by the third-order Birch-Murnaghan (B-M) equation of state

$$P(V) = \frac{3B_0}{2}\left[\left(\frac{V_0}{V}\right)^{\frac{7}{3}} - \left(\frac{V_0}{V}\right)^{\frac{5}{3}}\right]\left\{1 + \frac{3}{4}\left(B' - 4\right)\left[\left(\frac{V_0}{V}\right)^{\frac{2}{3}} - 1\right]\right\} \quad (5)$$

where $V_0$ is the zero-pressure volume, $B_0$ is the bulk modulus, and $B'$ is the parameter for the pressure derivative. For the structural comparisons, $B'$ is fixed at 4.

### *Calibration of pressure using emission line of ruby sphere*

The measurement of ruby fluorescence and sample photoluminescence at the same time. There are two emission lines in ruby fluorescence, and the prime one is the so-called $R_1$ ruby fluorescence line (*72*). The $R_1$ line shows a roughly linear dependence on pressure. Therefore, the spectral position of the $R_1$ line can be used to obtain the pressure using the empirical equation as follows (*73*, *74*)

$$P(\mathrm{GPa}) = \frac{1904}{B}\left[\left(1 + \frac{\Delta\lambda}{\lambda_0}\right)^B - 1\right] \quad (6)$$

where $\lambda_0$ is the wavelength of the $R_1$ line near 694.25 nm under ambient conditions and $\Delta\lambda$ is the difference value between the measured wavelength $\lambda$ and the initial wavelength $\lambda_0$.

### *Details of PLQYs calculation under pressure*

The PLQY can be calculated using the following equation (*46*)

$$\Phi = \Phi_R \frac{\int F(\lambda_{em})}{\int F_R(\lambda_{em})} \frac{A_R(\lambda_{ex})}{A(\lambda_{ex})} \frac{n^2}{n_R^2} \quad (7)$$

where $\Phi$ is the PLQY, $\int F(\lambda_{em})$ is the integrated intensity of emission, $A$ is the absorbance at the excitation wavelength, $n$ is the refractive index, and the subscript $R$ denotes the reference data at ambient pressure.

$n$ can be estimated from the Clausius-Mossotti equation and Lorentz-Lorenz equation

$$\frac{n^2 - 1}{n^2 + 2} \cdot \frac{1}{\rho} = \frac{4\pi}{3} \cdot N_A \cdot \alpha = R_{LL} \quad (8)$$

in which the density $\rho$ can be calculated from the cell volume. $R_{LL}$ is called the Lorentz-Lorenz constant. $R_{LL}$ is related to polarizability $\alpha$.

## Supplementary Materials

**This PDF file includes:**

Figs. S1 to S52
Tables S1 to S13
References

## REFERENCES AND NOTES


1. M. Walter, J. Akola, O. Lopez-Acevedo, P. D. Jadzinsky, G. Calero, C. J. Ackerson, R. L. Whetten, H. Grönbeck, H. Häkkinen, A unified view of ligand-protected gold clusters as superatom complexes. *Proc. Natl. Acad. Sci. U.S.A.* **105**, 9157–9162 (2008).
2. Y. Hua, Z.-H. Shao, A. Zhai, L.-J. Zhang, Z.-Y. Wang, G. Zhao, F. Xie, J.-Q. Liu, X. Zhao, X. Chen, S.-Q. Zang, Water-soluble $Au_{25}$ clusters with single-crystal structure for mitochondria-targeting radioimmunotherapy. *ACS Nano* **17**, 7837–7846 (2023).
3. Y.-J. Kong, J.-H. Hu, X.-Y. Dong, Y. Si, Z.-Y. Wang, X.-M. Luo, H.-R. Li, Z. Chen, S.-Q. Zang, T. C. W. Mak, Achiral-Core-Metal change in isomorphic enantiomeric $Ag_{12}Ag_{32}$ and $Au_{12}Ag_{32}$ clusters triggers circularly polarized phosphorescence. *J. Am. Chem. Soc.* **144**, 19739–19747 (2022).
4. H. Ma, X. Zhang, L. Liu, Y. Huang, S. Sun, K. Chen, Q. Xin, P. Liu, Y. Yan, Y. Wang, Y. Li, H. Liu, R. Zhao, K. Tan, X. Chen, X. Yuan, Y. Li, Y. Liu, H. Dai, C. Liu, H. Wang, X.-D. Zhang, Bioactive NIR-II gold clusters for three-dimensional imaging and acute inflammation inhibition. *Sci. Adv.* **9**, eadh7828 (2023).
5. J.-Q. Wang, R.-L. He, W.-D. Liu, Q.-Y. Feng, Y.-E. Zhang, C.-Y. Liu, J.-X. Ge, Q.-M. Wang, Integration of metal catalysis and organocatalysis in a metal nanocluster with anchored proline. *J. Am. Chem. Soc.* **145**, 12255–12263 (2023).
6. Y. Zhong, J. Zhang, T. Li, W. Xu, Q. Yao, M. Lu, X. Bai, Z. Wu, J. Xie, Y. Zhang, Suppression of kernel vibrations by layer-by-layer ligand engineering boosts photoluminescence efficiency of gold nanoclusters. *Nat. Commun.* **14**, 658 (2023).
7. S. Muramatsu, Y. Nakahigashi, T. Omoda, S. Takano, T. Tsukuda, Y. Inokuchi, Collision-induced fission of oblate gold superatom in $[Au_9(PPh_3)_8]^{3+}$: Deformation-mediated mechanism. *J. Phys. Chem. Lett.* **14**, 5641–5647 (2023).
8. L. Luo, Z. Liu, A. Mazumder, R. Jin, Raising Near-infrared photoluminescence quantum yield of $Au_{42}$ quantum rod to 50% in solutions and 75% in films. *J. Am. Chem. Soc.* **146**, 27993–27997 (2024).
9. P. Luo, X.-J. Zhai, S. Bai, Y.-B. Si, X.-Y. Dong, Y.-F. Han, S.-Q. Zang, Highly efficient circularly polarized luminescence from chiral $Au_{13}$ clusters stabilized by enantiopure monodentate NHC ligands. *Angew. Chem. Int. Ed.* **62**, e202219017 (2023).
10. M. R. Narouz, S. Takano, P. A. Lummis, T. I. Levchenko, A. Nazemi, S. Kaappa, S. Malola, G. Yousefalizadeh, L. A. Calhoun, K. G. Stamplecoskie, H. Häkkinen, T. Tsukuda, C. M. Crudden, Robust, Highly luminescent $Au_{13}$ superatoms protected by N-heterocyclic carbenes. *J. Am. Chem. Soc.* **141**, 14997–15002 (2019).
11. Y. Wang, Z. Liu, A. Mazumder, C. G. Gianopoulos, K. Kirschbaum, L. A. Peteanu, R. Jin, Tailoring carbon tails of ligands on $Au_{52}(SR)_{32}$ nanoclusters enhances the near-infrared photoluminescence quantum yield from 3.8 to 18.3%. *J. Am. Chem. Soc.* **145**, 26328–26338 (2023).

12. J. Xin, J. Xu, C. Zhu, Y. Tian, Q. Zhang, X. Kang, M. Zhu, Restriction of intramolecular rotation for functionalizing metal nanoclusters. *Chem. Sci.* **14**, 8474–8482 (2023).
13. K. Konishi, M. Iwasaki, Y. Shichibu, Phosphine-ligated gold clusters with core+*exo* geometries: Unique properties and interactions at the ligand–cluster interface. *Acc. Chem. Res.* **51**, 3125–3133 (2018).
14. S. Wang, X. Meng, A. Das, T. Li, Y. Song, T. Cao, X. Zhu, M. Zhu, R. Jin, A 200-fold quantum yield boost in the photoluminescence of silver-doped $Ag_xAu_{25-x}$ nanoclusters: The 13th silver atom matters. *Angew. Chem. Int. Ed.* **53**, 2376–2380 (2014).
15. W.-Q. Shi, L. Zeng, R.-L. He, X.-S. Han, Z.-J. Guan, M. Zhou, Q.-M. Wang, Near-unity NIR phosphorescent quantum yield from a room-temperature solvated metal nanocluster. *Science* **383**, 326–330 (2024).
16. Z. Liu, M. Zhou, L. Luo, Y. Wang, E. Kahng, R. Jin, Elucidating the near-infrared photoluminescence mechanism of homometal and doped $M_{25}(SR)_{18}$ nanoclusters. *J. Am. Chem. Soc.* **145**, 19969–19981 (2023).
17. H. Hirai, S. Takano, T. Nakashima, T. Iwasa, T. Taketsugu, T. Tsukuda, Doping-mediated energy-level engineering of $M@Au_{12}$ superatoms (M=Pd, Pt, Rh, Ir) for efficient photoluminescence and photocatalysis. *Angew. Chem. Int. Ed. Engl.* **61**, e202207290 (2022).
18. W.-M. He, J.-H. Hu, Y.-J. Cui, J. Li, Y.-B. Si, S.-B. Wang, Y.-J. Zhao, Z. Zhou, L.-F. Ma, S.-Q. Zang, Filling the gaps in icosahedral superatomic metal clusters. *Natl. Sci. Rev.* **11**, nwae174 (2024).
19. Y. Zhang, W. Zhang, T.-S. Zhang, C. Ge, Y. Tao, W. Fei, W. Fan, M. Zhou, M.-B. Li, Site-recognition-induced structural and photoluminescent evolution of the gold–pincer nanocluster. *J. Am. Chem. Soc.* **146**, 9631–9639 (2024).
20. K. Sheng, Z. Wang, L. Li, Z.-Y. Gao, C.-H. Tung, D. Sun, Solvent-mediated separation and reversible transformation of 1D supramolecular polymorphs built from $[W_{10}O_{32}]^{4-}$ templated 48-nuclei silver(I) cluster. *J. Am. Chem. Soc.* **145**, 10595–10603 (2023).
21. Z. Han, Y. Si, X.-Y. Dong, J.-H. Hu, C. Zhang, X.-H. Zhao, J.-W. Yuan, Y. Wang, S.-Q. Zang, Smart reversible transformations between chiral superstructures of copper clusters for optical and chiroptical switching. *J. Am. Chem. Soc.* **145**, 6166–6176 (2023).
22. B.-L. Han, Z. Liu, L. Feng, Z. Wang, R. K. Gupta, C. M. Aikens, C.-H. Tung, D. Sun, Polymorphism in atomically precise $Cu_{23}$ nanocluster incorporating tetrahedral $[Cu_4]^0$ kernel. *J. Am. Chem. Soc.* **142**, 5834–5841 (2020).
23. Y. Wang, S.-M. Zhai, P. Luo, X.-Y. Dong, J.-Y. Wang, Z. Han, S.-Q. Zang, Vapor- and temperature-triggered reversible optical switching for multi-response $Cu_8$ cluster supercrystals. *Chin. Chem. Lett.* **35**, 109493 (2024).
24. J. Wang, Z. Chai, J. Wang, C. Wang, M. Han, Q. Liao, A. Huang, P. Lin, C. Li, Q. Li, Z. Li, Mechanoluminescence or room-temperature phosphorescence: molecular packing-dependent emission response. *Angew. Chem. Int. Ed. Engl.* **58**, 17297–17302 (2019).
25. K. Zheng, F. Ni, Z. Chen, C. Zhong, C. Yang, Polymorph-dependent thermally activated delayed fluorescence emitters: understanding TADF from a perspective of aggregation state. *Angew. Chem. Int. Ed. Engl.* **59**, 9972–9976 (2020).
26. Q. Li, Z. Li, Molecular packing: Another key point for the performance of organic and polymeric optoelectronic materials. *Acc. Chem. Res.* **53**, 962–973 (2020).
27. Y. Chen, A. Li, X. Li, L. Tu, Y. Xie, S. Xu, Z. Li, Multi-stimuli-responsive amphiphilic pyridinium salt and its application in the visualization of level 3 details in latent fingerprints. *Adv. Mater.* **35**, e2211917 (2023).
28. H. Liu, Y. Gu, Y. Dai, K. Wang, S. Zhang, G. Chen, B. Zou, B. Yang, Pressure-induced blue-shifted and enhanced emission: A cooperative effect between aggregation-induced emission and energy-transfer suppression. *J. Am. Chem. Soc.* **142**, 1153–1158 (2020).
29. C. Li, K. Liu, H. Yan, L. Zhang, D. Jiang, T. Wen, B. Yue, Y. Wang, Lateral heterostructures fabricated via artificial pressure gradient. *Adv. Mater.* **36**, 2407922 (2024).
30. Y. Li, K. Wang, R. Feng, J. Wang, X.-J. Xi, F. Lang, Q. Li, W. Li, B. Zou, J. Pang, X.-H. Bu, Reticular modulation of piezofluorochromic behaviors in organic molecular cages by replacing non-luminous components. *Angew. Chem. Int. Ed.* **63**, e202403646 (2024).
31. A. Liang, J. Gonzalez-Platas, R. Turnbull, C. Popescu, I. Fernandez-Guillen, R. Abargues, P. P. Boix, L.-T. Shi, D. Errandonea, Reassigning the pressure-induced phase transitions of methylammonium lead bromide perovskite. *J. Am. Chem. Soc.* **144**, 20099–20108 (2022).
32. X. Yu, Y. Fang, X. Sun, Y. Xie, C. Liu, K. Wang, G. Xiao, B. Zou, Pressure-tuning localized excitons toward enhanced emission, photocurrent enhancement and piezochromism in unconventional ACI-type 2D hybrid perovskites. *Angew. Chem. Int. Ed.* **63**, e202412756 (2024).
33. L. Yue, Z. Li, L. Yu, K. Xu, R. Liu, C. Li, Y. Li, D. Yang, X. Li, Q. Li, B. Liu, Radical n–p conduction switching and significant photoconductivity enhancement in $NbOI_2$ via pressure-modulated peierls distortion. *J. Am. Chem. Soc.* **146**, 25245–25252 (2024).
34. Z. Zeng, J. Wen, H. Lou, X. Zhang, L. Yang, L. Tan, B. Cheng, X. Zuo, W. Yang, W. L. Mao, H.-K. Mao, Q. Zeng, Preservation of high-pressure volatiles in nanostructured diamond capsules. *Nature* **608**, 513–517 (2022).
35. L. Zhang, S. Li, H. Sun, Y. Fang, Y. Wang, K. Wang, H. Jiang, L. Sui, G. Wu, K. Yuan, B. Zou, Manipulating lone-pair-driven luminescence in 0D tin halides by pressure-tuned stereochemical activity from static to dynamic. *Angew. Chem. Int. Ed. Engl.* **62**, e202311912 (2023).
36. P. Zhang, D. Gao, X. Tang, X. Yang, H. Zheng, Y. Wang, X. Wang, J. Xu, Z. Wang, J. Liu, X. Wang, J. Ju, M. Tang, X. Dong, K. Li, H.-k. Mao, Ordered van der waals hetero-nanoribbon from pressure-induced topochemical polymerization of azobenzene. *J. Am. Chem. Soc.* **145**, 6845–6852 (2023).
37. K. Bu, X. Feng, D. Wang, T. Fu, Y. Ma, S. Guo, H. Luo, Y. Ding, T. Zhai, X. Lü, Quantifying structural polarization by continuous regulation of lone-pair electron expression in molecular crystals. *J. Am. Chem. Soc.* **146**, 22469–22475 (2024).
38. B. Xu, Y. Li, P. Hong, P. Zhang, J. Han, Z. Xiao, Z. Quan, Pressure-controlled free exciton and self-trapped exciton emission in quasi-one-dimensional hybrid lead bromides. *Nat. Commun.* **15**, 7403 (2024).
39. Q. Yang, X. Yang, Y. Wang, Y. Fei, F. Li, H. Zheng, K. Li, Y. Han, T. Hattori, P. Zhu, S. Zhao, L. Fang, X. Hou, Z. Liu, B. Yang, B. Zou, Brightening triplet excitons enable high-performance white-light emission in organic small molecules via integrating $n$–$\pi^*$/$\pi$–$\pi^*$ transitions. *Nat. Commun.* **15**, 7778 (2024).
40. D. Zhang, B. Fu, W. He, H. Li, F. Liu, L. Wang, H. Liu, L. Zhou, W. Cai, Pressure-induced shape and color changes and mechanical-stimulation-driven reverse transition in a one-dimensional hybrid halide. *Nat. Commun.* **15**, 6678 (2024).
41. Q. Li, C. J. Zeman IV, B. Kalkan, K. Kirschbaum, C. G. Gianopoulos, A. Parakh, D. Doan, A. C. Lee, J. Kulikowski, G. C. Schatz, G. Shen, M. Kunz, X. W. Gu, Direct observation of the pressure-induced structural variation in gold nanoclusters and the correlated optical response. *Nano Lett.* **23**, 132–139 (2023).
42. Q. Li, M. A. Mosquera, L. O. Jones, A. Parakh, J. Chai, R. Jin, G. C. Schatz, X. W. Gu, Pressure-induced optical transitions in metal nanoclusters. *ACS Nano* **14**, 11888–11896 (2020).
43. N. Kobayashi, Y. Kamei, Y. Shichibu, K. Konishi, Protonation-induced chromism of pyridylethynyl-appended [core+*exo*]-type $Au_8$ clusters. Resonance-coupled electronic perturbation through $\pi$-conjugated group. *J. Am. Chem. Soc.* **135**, 16078–16081 (2013).
44. Q. Liao, Q. Li, Z. Li, The key role of molecular packing in luminescence property: From adjacent molecules to molecular aggregates. *Adv. Mater.* , 2306617 (2023).
45. W. Chen, Z. Chen, Y. Chi, W. Tian, Double cation–$\pi$ directed two-dimensional metallacycle-based hierarchical self-assemblies for dual-mode catalysis. *J. Am. Chem. Soc.* **145**, 19746–19758 (2023).
46. Y. Wang, S. Guo, H. Luo, C. Zhou, H. Lin, X. Ma, Q. Hu, M.-h. Du, B. Ma, W. Yang, X. Lü, Reaching 90% photoluminescence quantum yield in one-dimensional metal halide $C_4N_2H_{14}PbBr_4$ by pressure-suppressed nonradiative loss. *J. Am. Chem. Soc.* **142**, 16001–16006 (2020).
47. M.-E. Sun, Y. Wang, F. Wang, J. Feng, L. Wang, H. Gao, G. Chen, J. Gu, Y. Fu, K. Bu, T. Fu, J. Li, X. Lü, L. Jiang, Y. Wu, S.-Q. Zang, Chirality-dependent structural transformation in chiral 2D perovskites under high pressure. *J. Am. Chem. Soc.* **145**, 8908–8916 (2023).
48. X.-J. Zhang, M.-E. Sun, F. Sun, Y. Jin, X.-Y. Dong, S. Li, H.-Y. Li, G. Chen, Y. Fu, Y. Wang, Q. Tang, Y. Wu, L. Jiang, S.-Q. Zang, Vibration-dependent dual-phosphorescent $Cu_4$ nanocluster with remarkable piezochromic behavior. *Angew. Chem. Int. Ed. Engl.* **63**, e202401724 (2024).
49. W. Gu, Y. Zhou, W. Wang, Q. You, W. Fan, Y. Zhao, G. Bian, R. Wang, L. Fang, N. Yan, N. Xia, L. Liao, Z. Wu, Concomitant near-infrared photothermy and photoluminescence of rod-shaped $Au_{52}(PET)_{32}$ and $Au_{66}(PET)_{38}$ synthesized concurrently. *Angew. Chem. Int. Ed. Engl.* **63**, e202407518 (2024).
50. M. Kato, Y. Shichibu, K. Ogura, M. Iwasaki, M. Sugiuchi, K. Konishi, I. Yagi, Terahertz raman spectroscopy of ligand-protected $Au_8$ clusters. *J. Phys. Chem. Lett.* **11**, 7996–8001 (2020).
51. J. Clark, T. Nelson, S. Tretiak, G. Cirmi, G. Lanzani, Femtosecond torsional relaxation. *Nat. Phys.* **8**, 225–231 (2012).
52. T. Jia, Z.-J. Guan, C. Zhang, X.-Z. Zhu, Y.-X. Chen, Q. Zhang, Y. Yang, D. Sun, Eight-electron superatomic $Cu_{31}$ nanocluster with chiral kernel and NIR-II emission. *J. Am. Chem. Soc.* **145**, 10355–10363 (2023).
53. Q. Li, M. Zhou, W. Y. So, J. Huang, M. Li, D. R. Kauffman, M. Cotlet, T. Higaki, L. A. Peteanu, Z. Shao, R. Jin, A mono-cuboctahedral series of gold nanoclusters: Photoluminescence origin, large enhancement, wide tunability, and structure–Property correlation. *J. Am. Chem. Soc.* **141**, 5314–5325 (2019).
54. K.-K. Tan, D.-W. Zhang, W.-L. Zhao, M. Li, C.-F. Chen, Axially chiral TADF-active materials with $\pi$-extended acceptors for highly efficient circularly polarized electroluminescence. *Chem. Eng. J.* **462**, 142123 (2023).
55. H. Lu, B. Chen, Y. Li, J. Shi, J. Li, L. Wang, S. Luo, C. Fan, J. Shen, J. Chen, Benzyl-rich ligand engineering of the photostability of atomically precise gold nanoclusters. *Chem. Commun.* **58**, 2395–2398 (2022).
56. Y.-M. Wang, F.-Q. Yan, Q.-Y. Wang, C.-X. Du, L.-Y. Wang, B. Li, S. Wang, S.-Q. Zang, Single-atom tailored atomically-precise nanoclusters for enhanced electrochemical reduction of $CO_2$-to-CO activity. *Nat. Commun.* **15**, 1843 (2024).
57. Y. Kamei, Y. Shichibu, K. Konishi, Generation of small gold clusters with unique geometries through cluster-to-cluster transformations: Octanuclear clusters with edge-sharing gold tetrahedron motifs. *Angew. Chem. Int. Ed. Engl.* **50**, 7442–7445 (2011).
58. CrysAlisPro, Agilent Technologies version 1.171.36.31 (2012).
59. G. M. Sheldrick, A short history of *SHELX*. *Acta Crystallogr. A* **64**, 112–122 (2008).

60. O. V. Dolomanov, L. J. Bourhis, R. J. Gildea, J. A. K. Howard, H. Puschmann, *OLEX2*: A complete structure solution, refinement and analysis program. *J. Appl. Cryst.* **42**, 339–341 (2009).
61. G. M. Sheldrick, Crystal structure refinement with *SHELXL*. *Acta. Cryst. C* **71**, 3–8 (2015).
62. L. J. Bourhis, O. V. Dolomanov, R. J. Gildea, J. A. K. Howardd, H. Puschmannb, The anatomy of a comprehensive constrained, restrained refinement program for the modern computing environment - *Olex2* dissected. *Acta Crystallogr. A Found Adv.* **71**, 59–75 (2015).
63. D. Errandonea, Y. Meng, M. Somayazulu, D. Häusermann, Pressure-induced $\alpha \rightarrow \omega$ transition in titanium metal: A systematic study of the effects of uniaxial stress. *Phys. B Condens. Matter* **355**, 116–125 (2005).
64. F. Neese, Software update: The ORCA program system, version 4.0. *Wiley Interdiscip. Rev. Comput. Mol. Sci.* **8**, e1327 (2018).
65. J. P. Perdew, K. Burke, M. Ernzerhof, Generalized gradient approximation made simple. *Phys. Rev. Lett.* **78**, 1396 (1997).
66. F. Weigend, R. Ahlrichs, Balanced basis sets of split valence, triple zeta valence and quadruple zeta valence quality for H to Rn: Design and assessment of accuracy. *Phys. Chem. Chem. Phys.* **7**, 3297–3305 (2005).
67. S. Grimme, S. Ehrlich, L. Goerigk, Effect of the damping function in dispersion corrected density functional theory. *J. Comput. Chem.* **32**, 1456–1465 (2011).
68. S. Grimme, J. Antony, S. Ehrlich, H. Krieg, A consistent and accurate ab initio parametrization of density functional dispersion correction (DFT-D) for the 94 elements H-Pu. *J. Chem. Phys.* **132**, 154104 (2010).
69. J. P. Perdew, S. Kurth, A. Zupan, P. Blaha, Accurate density functional with correct formal properties: A step beyond the generalized gradient approximation. *Phys. Rev. Lett.* **82**, 2544–2547 (1999).
70. B. A. Hess, C. M. Marian, U. Wahlgren, O. Gropen, A mean-field spin-orbit method applicable to correlated wavefunctions. *Chem. Phys. Lett.* **251**, 365–371 (1996).
71. Z. Wang, A. Hao, P. Xing, Halogen interaction effects on chiral self-assemblies on cyclodipeptide scaffolds across hierarchy. *Small* **19**, e2302517 (2023).
72. H. K. Mao, P. M. Bell, J. W. Shaner, D. J. Steinberg, Specific volume measurements of Cu, Mo, Pd, and Ag and calibration of the ruby $R_1$ fluorescence pressure gauge from 0.06 to 1 Mbar. *J. Appl. Phys.* **49**, 3276–3283 (1978).
73. K. Syassen, Ruby under pressure. *High Pressure Res.* **28**, 75–126 (2008).
74. J. C. Chervin, B. Canny, M. Mancinelli, Ruby-spheres as pressure gauge for optically transparent high pressure cells. *High Pressure Res.* **21**, 305–314 (2001).
75. Z. Lei, X.-L. Pei, Z.-J. Guan, Q.-M. Wang, Full protection of intensely luminescent gold(I)–silver(I) cluster by phosphine ligands and inorganic anions. *Angew. Chem. Int. Ed.* **56**, 7117–7120 (2017).
76. X.-M. Wu, J.-Y. Wang, Y.-Z. Huang, Z.-N. Chen, Scissor-like $Au_4Cu_2$ cluster with phosphorescent mechanochromism and thermochromism. *Molecules* **28**, 3247 (2023).
77. Z. Han, X. Zhao, P. Peng, S. Li, C. Zhang, M. Cao, K. Li, Z.-Y. Wang, S.-Q. Zang, Intercluster aurophilicity-driven aggregation lighting circularly polarized luminescence of chiral gold clusters. *Nano Res.* **13**, 3248–3252 (2020).
78. S.-S. Zhang, L. Feng, R. D. Senanayake, C. M. Aikens, X.-P. Wang, Q.-Q. Zhao, C.-H. Tung, D. Sun, Diphosphine-protected ultras mall gold nanoclusters: Opened icosahedral $Au_{13}$ and heart-shaped $Au_8$ clusters. *Chem. Sci.* **9**, 1251–1258 (2018).
79. M. Bai, L. Qin, X.-M. Zeng, M. Wu, L.-Y. Yao, G.-Y. Yang, Dithiocarbonate-protected $Au_{25}$ nanorods of a chiral $D_5$ configuration and NIR-II phosphorescence. *J. Am. Chem. Soc.* **146**, 12734–12742 (2024).
80. Z.-M. Zhu, Y. Zhao, H. Zhao, C. Liu, Y. Zhang, W. Fei, H. Bi, M.-B. Li, Photochemical route for synthesizing atomically precise metal nanoclusters from disulfide. *Nano Lett.* **23**, 7508–7515 (2023).
81. Z. Liu, L. Luo, J. Kong, E. Kahng, M. Zhou, R. Jin, Bright near-infrared emission from the $Au_{39}(SR)_{29}$ nanocluster. *Nanoscale* **16**, 7419–7426 (2024).
82. H. Hirai, T. Nakashima, S. Takano, Y. Shichibu, K. Konishi, T. Kawai, T. Tsukuda, $IrAu_{12}$ superatom modified by chiral diphosphines: Doping-induced enhancement of chiroptical activity. *J. Mater. Chem. C* **11**, 3095–3100 (2023).
83. A. Ma, J. Wang, J. Kong, Y. Ren, Y. Wang, X. Ma, M. Zhou, S. Wang, $Au_{10}Ag_{17}(TPP)_{10}(SR)_6Cl_5$ nanocluster: Structure, transformation and the origin of its photoluminescence. *Phys. Chem. Chem. Phys.* **25**, 9772–9778 (2023).
84. Q. Li, C. J. I. V. Zeman, G. C. Schatz, X. W. Gu, Source of bright near-infrared luminescence in gold nanoclusters. *ACS Nano* **15**, 16095–16105 (2021).
85. X.-K. Wan, W. W. Xu, S.-F. Yuan, Y. Gao, X.-C. Zeng, Q.-M. Wang, A near-infrared-emissive alkynyl-protected $Au_{24}$ nanocluster. *Angew. Chem. Int. Ed.* **54**, 9683–9686 (2015).
86. Q. Li, C. J. Zeman IV, Z. Ma, G. C. Schatz, X. W. Gu, Bright NIR-II photoluminescence in rod-shaped icosahedral gold nanoclusters. *Small* **17**, e2007992 (2021).
87. Y. Yu, Z. Luo, D. M. Chevrier, D. T. Leong, P. Zhang, D.-e. Jiang, J. Xie, Identification of a highly luminescent $Au_{22}(SG)_{18}$ nanocluster. *J. Am. Chem. Soc.* **136**, 1246–1249 (2014).
88. Z. Gan, Y. Lin, L. Luo, G. Han, W. Liu, Z. Liu, C. Yao, L. Weng, L. Liao, J. Chen, X. Liu, Y. Luo, C. Wang, S. Wei, Z. Wu, Fluorescent gold nanoclusters with interlocked staples and a fully thiolate-bound kernel. *Angew. Chem. Int. Ed.* **55**, 11567–11571 (2016).
89. W.-D. Si, C. Zhang, M. Zhou, W.-D. Tian, Z. Wang, Q. Hu, K.-P. Song, L. Feng, X.-Q. Huang, Z.-Y. Gao, C.-H. Tung, D. Sun, Two triplet emitting states in one emitter: Near-infrared dual-phosphorescent $Au_{20}$ nanocluster. *Sci. Adv.* **9**, eadg3587 (2023).
90. J. Dong, Z. Gan, W. Gu, Q. You, Y. Zhao, J. Zha, J. Li, H. Deng, N. Yan, Z. Wu, Synthesizing photoluminescent $Au_{28}(SCH_2Ph\text{-}^tBu)_{22}$ nanoclusters with structural features by using a combined method. *Angew. Chem. Int. Ed.* **60**, 17932–17936 (2021).
91. A. Mazumder, K. Li, Z. Liu, Y. Wang, Y. Pei, L. A. Peteanu, R. Jin, Isomeric effects of $Au_{28}(S\text{-}c\text{-}C_6H_{11})_{20}$ nanoclusters on photoluminescence: Roles of electron-vibration coupling and higher triplet state. *ACS Nano* **18**, 21534–21543 (2024).
92. L. Luo, Z. Liu, X. Du, R. Jin, Photoluminescence of the $Au_{38}(SR)_{26}$ nanocluster comprises three radiative processes. *Comm. Chem.* **6**, 22 (2023).
93. S. Takano, H. Hirai, T. Nakashima, T. Iwasa, T. Taketsugu, T. Tsukuda, Photoluminescence of doped superatoms M@$Au_{12}$ (M = Ru, Rh, Ir) homoleptically capped by $(Ph_2)PCH_2P(Ph_2)$: Efficient room-temperature phosphorescence from Ru@$Au_{12}$. *J. Am. Chem. Soc.* **143**, 10560–10564 (2021).
94. X.-K. Wan, X.-S. Han, Z.-J. Guan, W.-Q. Shi, J.-J. Li, Q.-M. Wang, Interplay of kernel shape and surface structure for NIR luminescence in atomically precise gold nanorods. *Nat. Commun.* **15**, 7214 (2024).


**Acknowledgments:** We appreciate the assistance of J. Li from Xuchang University in the calculations during the revision process. **Funding:** This work was supported by the National Natural Science Foundation of China (nos. 92461304 to S.-Q. Z., 52103238 to G. C., 92356304 to S.-Q. Z., 92061201 to S.-Q. Z., 21825106 to S.-Q. Z.), the China Postdoctoral Science Foundation (nos. 2021TQ0289 to G. C. and 2021 M700128 to G.C.), the National Key R&D Program of China (2021YFA1200300 to S.-Q. Z.), the Zhongyuan Thousand Talents (Zhongyuan Scholars) Program of Henan Province (234000510007 to S.-Q. Z.), and the Zhengzhou University. The in situ high-pressure PXRD was performed at 4W2 HP-Station in the Beijing Synchrotron Radiation Facility (BSRF) and BL15U1 Station in the Shanghai Synchrotron Radiation Facility (SSRF). **Author contributions:** Conceptualization: G.C. and S.-Q.Z. Methodology: G.C., S.-Q.Z., H.-Y.R., J.-K.Y., Q.L., J.L., and G.L. Software: G.C., S.-Q. Z., H.-Y.R., J.-K.Y., J.L., and G.L. Validation: G.C., S.-Q.Z., H.-Y.R., J.-K.Y., Y.-N.Y., Q.-Y.W., M.-J.Z., Y.Wu., J.L., J.-H.H., G.L., and L.J. Formal analysis: G.C., S.-Q.Z., H.-Y.R., J.-K.Y., Y.-N.Y., Q.-Y.W., M.-J.Z., Y.Wu., M.Z., J.L., J.-H.H., G.L., and L.J. Investigation: G.C., S.-Q.Z., H.-Y.R., J.-K.Y., Y.-N.Y., Q.-Y.W., M.-J.Z., Q.L., Y.Wu., M.Z., J.L., J.-H.H., G.L., Y.Wa., L.J. Resources: G.C., S.-Q.Z., J.L., G.L., Y.Wa. Data curation: G.C., S.-Q.Z., H.-Y.R., J.-K.Y., Y.-N.Y., Q.-Y.W., M.-J.Z., Y.Wu., J.L., J.-H.H., G.L., and L.J. Writing—original draft: G.C., S.-Q.Z., and H.-Y.R. Writing—review and editing: G.C., S.-Q.Z., H.-Y.R., J.-K.Y., Y.-N.Y., Q.-Y.W., M.-J.Z., Q.L., Y.Wu., M.Z., J.L., J.-H.H., G.L., Y.Wa., and L.J. Visualization: G.C., S.-Q.Z., H.-Y.R., J.-K.Y., J.L., and G.L. Supervision: G.C., S.-Q.Z., Q.L., J.L., and G.L. Project administration: G.C., S.-Q.Z., J.L., and G.L. Funding acquisition: G.C., S.-Q.Z., J.L., and G.L. **Competing interests:** The authors declare that they have no competing interests. **Data and materials availability:** All data needed to evaluate the conclusions in the paper are present in the paper and/or the Supplementary Materials. The cif. data of $Au_8$-P can be obtained free of charge from The Cambridge Crystallographic Data Centre (CCDC) with access code CCDC 2404807 of $Au_8$-P.

Submitted 5 December 2024
Accepted 25 April 2025
Published 30 May 2025
10.1126/sciadv.adv0298